

A Cyanopolyyne-rich but Complex-organic-molecule-poor Massive Protostar: The First Hot Carbon-chain Chemistry Source G28.28-0.36

Downloaded from: https://research.chalmers.se, 2026-11-24 19:19 UTC

Citation for the original published paper (version of record):
Taniguchi, K., Saito, M., Gorai, P. et al (2026). A Cyanopolyyne-rich but Complex-organic-molecule-poor Massive Protostar: The First Hot Carbon-chain Chemistry Source G28.28-0.36. Astrophysical Journal, 1011(2).
http://dx.doi.org/10.3847/1538-4357/aeacdb

N.B. When citing this work, cite the original published paper.

research.chalmers.se offers the possibility of retrieving research publications produced at Chalmers University of Technology. It covers all kind of research output: articles, dissertations, conference papers, reports etc. since 2004. research.chalmers.se is administrated and maintained by Chalmers Library

(article starts on next page)

The Astrophysical Journal, 1011:163 (14pp), 2026 November 10 https://doi.org/10.3847/1538-4357/aeacdb
© 2026. The Author(s). Published by the American Astronomical Society.
OPEN ACCESS

A Cyanopolyyne-rich but Complex-organic-molecule-poor Massive Protostar: The First Hot Carbon-chain Chemistry Source G28.28-0.36

Kotomi Taniguchi[1,2], Masao Saito[1,2], Prasanta Gorai[3,4,5], Olli Sipilä[6], Kazuhito Dobashi[7], Paola Caselli[6], Tirupati Kumara Sridharan[8], Tomomi Shimoikura[9], and Jonathan C. Tan[10,11]
[1] National Astronomical Observatory of Japan, National Institutes of Natural Sciences, 2-21-1, Osawa, Mitaka, Tokyo 181-8588, Japan; kotomi.taniguchi@nao.ac.jp
[2] Astronomical Science Program, The Graduate University for Advanced Studies, SOKENDAI, 2-21-1 Osawa, Mitaka, Tokyo 181-8588, Japan
[3] Rosseland Centre for Solar Physics, University of Oslo, PO Box 1029 Blindern, 0315 Oslo, Norway
[4] Institute of Theoretical Astrophysics, University of Oslo, PO Box 1029 Blindern, 0315 Oslo, Norway
[5] Universität Heidelberg, Zentrum für Astronomie, Institut für Theoretische Astrophysik, Albert-Ueberle-Str. 2, 69120 Heidelberg, Germany
[6] Max-Planck-Institut für extraterrestrische Physik, Gießenbachstrasse, 85748 Garching bei München, Germany
[7] Tokyo Gakugei University, Koganei, Tokyo 184-8501, Japan
[8] National Radio Astronomy Observatory, 520 Edgemont Road, Charlottesville, VA, USA
[9] Otsuma Women's University Chiyoda, Tokyo 102-8357, Japan
[10] Department of Physics and Astronomy, Chalmers University of Technology, 412 93 Gothenburg, Sweden
[11] Department of Astronomy, University of Virginia, Charlottesville, VA 22904, USA
Received 2026 May 10; revised 2026 September 24; accepted 2026 September 24; published 2026 November 2

Abstract

We present molecular emission line data from the massive young stellar object (MYSO) G28.28-0.36 (G28.28) obtained with the Atacama Large Millimeter/submillimeter Array Band 3. Cyanopolyynes (HC_3N and HC_5N) and three complex organic molecules (COMs; CH_3OH, CH_3CN, and CH_3CHO) are detected from the MYSO G28.28. In addition, strong emission regions of cyanopolyynes are identified between G28.28 and a nearby ultracompact H II region. The HC_5N emission is coincident with the dust continuum peak, where an excitation temperature of 100 K is derived from CH_3CN. These results suggest that the hot carbon-chain chemistry (HCCC) mechanism produces cyanopolyynes in the hot region around G28.28. We find that G28.28 exhibits a unique chemical feature: cyanopolyynes are abundant, but COMs are deficient, unlike the other MYSOs studied previously. These results imply that G28.28 is a counterpart of the warm carbon-chain chemistry (WCCC) low-mass source L1527. G28.28 is the first HCCC source identified so far.

Unified Astronomy Thesaurus concepts: Astrochemistry (75); Interstellar molecules (849); Massive stars (732)

1. Introduction

Chemical compositions around protostars are essential because they provide information on protostellar evolutionary stages, physical conditions (gas density, temperature), and the environments in which protostars formed. Chemical complexities in protostellar envelopes have been discovered, but their origins remain unclear. Saturated complex organic molecules (COMs), which consist of six atoms or more, at least one of which is carbon (E. Herbst & E. F. van Dishoeck 2009), are abundant in the hot ($T \geqslant 100$ K) gas around protostellar cores. These chemical features are known as "hot cores" and "hot corinos" for high-mass and low-mass protostars, respectively.

Unsaturated carbon-chain species have been known to be abundant in cold gas at the starless-core stage (e.g., H. Suzuki et al. 1992). These species mainly form via the bottom-up process starting from ionized carbon (C^+) and atomic carbon (C) in the cold gas (K. Taniguchi et al. 2024a and references therein). Another carbon-chain formation process has been found around the low-mass protostar L1527 in the Taurus star-forming region and was named warm carbon-chain chemistry (WCCC; N. Sakai et al. 2008). The detected carbon-chain emission comes from lukewarm envelopes around protostars with temperatures around 20–30 K. In the WCCC mechanism, the first step for carbon-chain formation is the gas-phase reaction between methane (CH_4), which sublimates from dust grains at ~25 K, and C^+ (G. E. Hassel et al. 2008). Recently, it has been found that the WCCC mechanism occurs around intermediate-mass protostars (K. Taniguchi et al. 2024b).

So far, carbon-chain chemistry has been studied mainly in nearby low-mass star-forming regions. The chemical evolution using carbon-chain species in high-mass star-forming regions was investigated with survey observations toward high-mass starless cores (HMSCs) and high-mass protostellar objects (HMPOs) using the Nobeyama 45 m radio telescope by K. Taniguchi et al. (2018b, 2019b). They found that HC_3N forms efficiently in lukewarm gas around early-stage HMPOs, which are still deeply embedded in dense gas and dust.

For later-stage high-mass sources, C.-E. Green et al. (2014) conducted survey observations of the HC_5N (J = 12–11; E_{up} = 9.96 K) line toward 79 hot cores associated with the 6.7 GHz methanol masers using the Tidbinbilla 34 m telescope. The line was detected from 35 sources. However, their detection does not ensure that the HC_5N emission comes from lukewarm envelopes and/or inner hot cores, because the detected line can be excited even in cold gas. K. Taniguchi et al. (2017) observed four massive young stellar objects (MYSOs) containing hot cores, which were selected from the source list of C.-E. Green et al. (2014), using the Green Bank 100 m and Nobeyama 45 m radio telescopes. They detected high-J lines (E_{up} = 63–100 K) that could not be excited in cold gas and obtained rotational temperatures of ~20–25 K. These

Original content from this work may be used under the terms of the Creative Commons Attribution 4.0 licence. Any further distribution of this work must maintain attribution to the author(s) and the title of the work, journal citation and DOI.

results suggest that the WCCC mechanism produces HC_5N even around MYSOs. These single-dish observations cannot resolve a hot-core (>100 K) region, and it was unclear whether HC_5N exists in the hot-core region yet. Follow-up observations show that G28.28-0.36 (hereafter G28.28) is the most HC_5N-rich but COM-poor MYSO among their sample (K. Taniguchi et al. 2018c, 2021).

Interferometric observations toward G28.28 were conducted using the Karl G. Jansky Very Large Array (VLA) in the Ka band (K. Taniguchi et al. 2018a). Some strong emission regions of cyanopolyynes (HC_3N and HC_5N) were found between G28.28 and a nearby ultracompact H II (UCH II) region, and these regions overlap with the 450 μm continuum emission. K. Taniguchi et al. (2018a) suggested that these regions harbor low-mass or intermediate-mass protostellar cores and the WCCC mechanism likely produces cyanopolyynes. However, the VLA observations did not cover high-J lines of cyanopolyynes, and therefore they could not trace the spatial distribution of a potential hot component of HC_5N.

K. Taniguchi et al. (2023a) analyzed Atacama Large Millimeter/submillimeter Array (ALMA) Band 3 data toward five MYSOs. The HC_5N (J = 35–34; E_{up} = 80.5 K) line was detected from three MYSOs where large nitrogen (N)-bearing COMs (CH_2CHCN and CH_3CH_2CN) were detected. They confirmed that the detected HC_5N emission arises from hot-core regions with temperatures above 100 K, where HC_5N sublimates from dust grains via thermal desorption. The formation process of cyanopolyynes in hot cores was named hot carbon-chain chemistry (HCCC; K. Taniguchi et al. 2023a). In the HCCC mechanism, cyanopolyynes form in lukewarm gas by the neutral–neutral reactions of "$C_{2n}H_2$ + CN" and accumulate into ice mantles (T < 100 K). After the temperature exceeds their sublimation temperatures (>100 K), they sublimate into the gas phase and reach their peak abundances in hot-core regions. Thus, their emission peaks are expected to be coincident with the continuum peaks associated with MYSOs. This study demonstrates that ALMA Band 3 observations are suitable for studying carbon-chain chemistry in hot regions.

The previous studies show that the chemical diversity arises not only in low-mass protostars but also in high-mass protostars. K. Taniguchi et al. (2024a) summarizes the chemical diversity based on stellar mass (see Figure 9 in their paper). The MYSOs studied by K. Taniguchi et al. (2023a) correspond to hybrid-type sources in which both cyanopolyynes and a variety of COMs coexist. However, no MYSO corresponding to the HCCC source, where cyanopolyynes are abundant but COMs are deficient in hot gas, has been discovered yet.[12] The MYSO G28.28 is the most promising candidate of an HCCC source (K. Taniguchi et al. 2024a), because COMs are much less abundant than in the other MYSOs (K. Taniguchi et al. 2018c). To confirm that G28.28 is a bona fide HCCC source, we need high angular resolution and high sensitivity data that spatially resolve molecular emission at a central hot-core region. In particular, information on the spatial distributions of the high-J HC_5N lines is necessary.

[12] The "HCCC mechanism" refers to the formation process of carbon-chain species that can proceed in both hybrid-type sources and HCCC sources. Here, we distinguish between hybrid-type and HCCC sources based on the categorization by K. Taniguchi et al. (2024a). The categorization was proposed as a counterpart to the low-mass case.

Table 1
Spectral Window Setup

Main Target Line	Center Frequency (GHz)	Bandwidth (MHz)
HC_5N (36–35)	95.840	62
CH_3CHO ($5_{0,5}$–$4_{0,4}$)	95.953	62
CH_3OH ($2_{1,2}$–$1_{1,1}$)	95.904	62
CH_3OH ($2_{1,1}$–$1_{1,0}$)	96.745	62
CH_3OCHO ($8_{3,6}$–$7_{3,5}$)	98.596	62
HC_5N (37–36)	98.502	62
CH_3CH_2CN ($12_{2,10}$–$11_{2,9}$)	108.929	62
HC_3N (12–11)	109.162	62
CH_3CN (J = 6–5)	110.363	62
Continuum	108.492	2000

In this paper, we present ALMA Band 3 data toward G28.28 (d = 3 kpc; C.-E. Green et al. 2014). The MYSO G28.28 has been identified as an extended green object (EGO)[13] associated with a likely MYSO outflow candidate (C. J. Cyganowski et al. 2008) and with a 6.7 GHz Class II CH_3OH maser (C. J. Cyganowski et al. 2009). The UCH II region G28.29-0.36 is located at $18^h44^m15\overset{s}{.}09$, $-4°17'54\overset{''}{.}9$ (J2000), corresponding to the east side of the MYSO G28.28 (C. J. Cyganowski et al. 2009).

This paper is organized as follows. Section 2 explains details of the observations with ALMA and the data reduction method. We present the results of a continuum image and moment 0 maps of detected molecular lines as well as their analyses in Section 3. The properties of the strong cyanopolyyne emission regions are discussed in Section 4.1. We compare the chemical compositions in some representative positions (Section 4.2) and between G28.28 and the other MYSOs studied by K. Taniguchi et al. (2023a) (Section 4.3). In Section 4.4, we summarize the chemical features of G28.28. Our main conclusions are summarized in Section 5.

2. Observations and Data Reduction

Observations were conducted during ALMA Cycle 10 (ID: 2023.1.00467.S., PI: Kotomi Taniguchi). The observations with the 12 m array were conducted in 2023 December and 2024 January, and those with the 7 m array were conducted in 2024 March. The center of the field of view (FoV) is set at the MYSO G28.28, whose coordinates are $18^h44^m13\overset{s}{.}3$, $-4°18'03\overset{''}{.}3$ (J2000). The synthesized beam size of the 12 m array is $1\overset{''}{.}54 \times 1\overset{''}{.}25$ (mean value is $1\overset{''}{.}39$), corresponding to ~0.02 pc at the source distance (3 kpc). The maximum recoverable scale and FoV size of the 12 m array are $19\overset{''}{.}2$ and $56\overset{''}{.}5$, respectively. The synthesized beam size of the 7 m array is $12\overset{''}{.}3$. The maximum recoverable scale of the 7 m array and FoV size are $83\overset{''}{.}3$ and $96\overset{''}{.}8$, respectively.

Table 1 summarizes the spectral window setup. Spectral windows targeting the molecular lines had a bandwidth of 62 MHz with a frequency resolution of 60.5 kHz, corresponding to a velocity resolution of ~0.17 km s^{-1} in the 3 mm band. One spectral window with a 2 GHz bandwidth was set at 108.492 GHz to improve the calibration.

[13] C. J. Cyganowski et al. (2008) identified extended 4.5 μm sources (EGOs) based on the Galactic Legacy Infrared Mid-Plane Survey Extraordinaire (GLIMPSE; R. A. Benjamin et al. 2003).

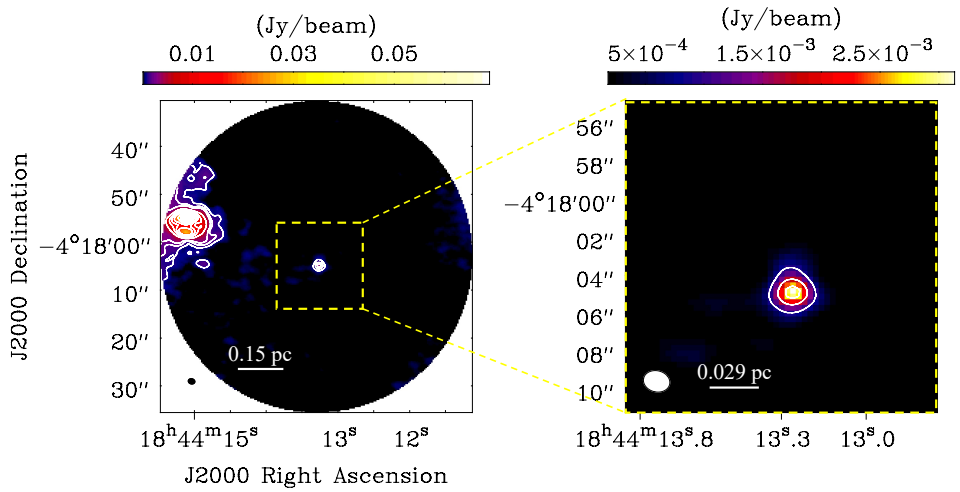

Figure 1. Continuum ($\lambda = 2.75$ mm) images toward the MYSO G28.28. The left panel shows the entire image, and the right panel shows a close-up image centered on the MYSO G28.28. The strong emission region at the east side in the left panel corresponds to the UCH II region G28.29-0.36. The noise level (1σ) is 0.18 mJy beam^{-1}. The contour levels in the left panel are 5σ, 10σ, 15σ, 35σ, 55σ, 75σ, 100σ, 150σ, 200σ, 250σ, 300σ, and 350σ, and those in the right panel are 5σ, 10σ, and 15σ.

We carried out data reduction using the Common Astronomy Software Applications package (CASA; CASA Team et al. 2022). We used the pipeline version 2023.1.0.124 with CASA 6.5.4.9. The continuum image and data cubes were created using the CASA tclean task, combining data of the 12 m and 7 m arrays. The pixel size was set at 0.″3. Briggs weighting (robust = 0.5) was applied. The final resulting beam size was 1.″4 × 1.″1, corresponding to 0.020 × 0.016 pc at the source distance.

3. Results and Analyses

3.1. Continuum Emission

Figure 1 shows the continuum ($\lambda = 2.75$ mm, corresponding to 108.9 GHz) image combining the 12 m and 7 m arrays. The MYSO G28.28 has been detected with a signal-to-noise ratio (S/N) well above 5σ.

We conducted the two-dimensional (2D) Gaussian fitting for the continuum source of the MYSO G28.28. The fitting results are summarized in Table 2. We constrained its stellar mass to 8–16$M_\odot$ with spectral energy distribution (SED) fitting (Figures A1 and A2 and Table A1 in Appendix A). The bolometric luminosity, core mass, and core radius are derived to be (1.9–5.2) × $10^4 L_\odot$, 100–480$M_\odot$, and 0.04–0.5 pc, respectively (Table A1 in Appendix A).

Table 2
Summary of the 2D Gaussian Fitting for G28.28 in the Continuum Image

Parameter	Value	Error
R.A. (J2000)	$18^h44^m13^s.262$	$0^s.003$
Dec. (J2000)	−4°18′04.″85	0.″05
Major axis FWHM [arcsec][a]	1.68	0.16
Minor axis FWHM [arcsec][a]	1.42	0.18
Position angle [deg][a]	163	149
Flux [mJy]	6.85	0.51
Peak [mJy beam^{-1}]	2.68	0.15

Note.
[a] Values are deconvolved from the beam.

3.2. Molecular Lines

3.2.1. Moment 0 Maps

Figure 2 shows moment 0 maps of the detected molecular lines. All of the lines have been detected at the continuum peak of the MYSO G28.28. Panels (a)–(c) show spatial distributions of cyanopolyynes (HC_3N and HC_5N). The HC_5N lines show a weak emission peak at the G28.28 continuum peak. The observed HC_5N lines have high E_{up} values (≈85 K), and their detection suggests that the emission arises from warm envelopes or hot ($T > 100$ K) gas. In addition to the G28.28 continuum peak, HC_3N and HC_5N show strong emission between the MYSO G28.28 and the UCH II region, even though no strong continuum peaks have been detected in the 2.75 mm continuum map (Figure 1). We will discuss the properties of the emission regions in Section 4.1.

The HC_3N emission also traces extended components. Diffuse components extending in the west–east direction centered on the MYSO G28.28 are detected. This feature may be related to extended envelope/cloud material and/or outflow activity. The HC_3N ($J = 11$–10) line has been reported as a potential tracer of low-velocity molecular outflows associated with massive protostars (A. Hoque et al. 2025). Although G28.28 has been identified as an EGO likely associated with outflow(s), the HC_3N moment 1 map and position–velocity diagram do not allow us to identify outflows unambiguously because of the complex velocity structure. Additional observations of dedicated jet/outflow tracers are needed to clarify the origin of the extended HC_3N emission.

In the case of COMs (CH_3CN, CH_3OH, and CH_3CHO), the emission between the MYSO G28.28 and the UCH II region is not as strong as for the cyanopolyynes, as shown in panels (d)–(g) of Figure 2. Strong emission peaks are detected at the northern part of the UCH II region. These peaks marginally correspond to the 2.75 mm continuum emission peaks. No source has yet been identified at the COM emission peaks located north of the UCH II region.

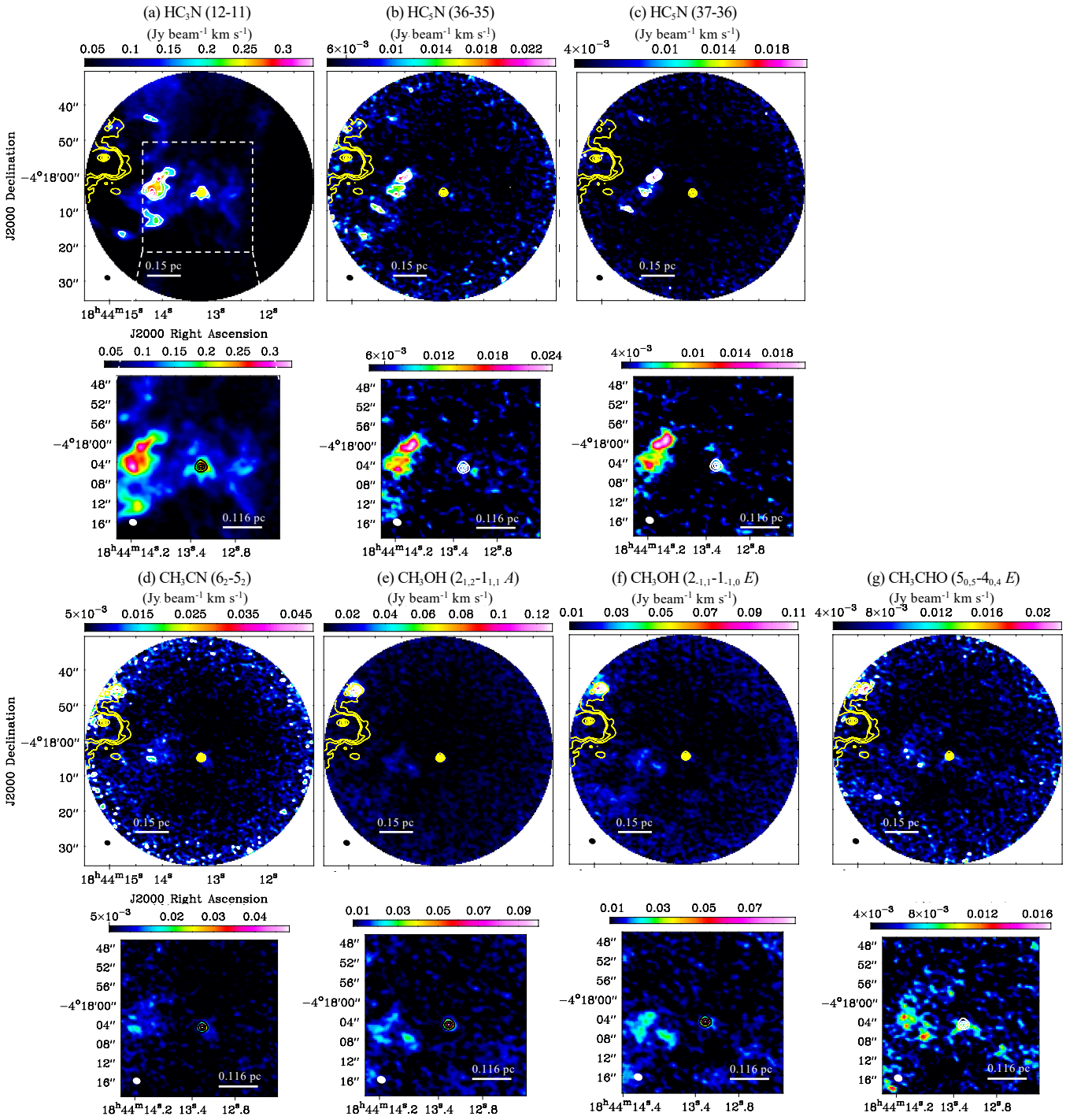

Figure 2. Moment 0 maps of the molecular lines. The upper three panels show maps of cyanopolyynes: (a) HC_3N ($J = 12$–11), (b) HC_5N ($J = 36 - 35$), and (c) HC_5N ($J = 37$–36). The lower four panels show maps of complex organic molecules: (d) CH_3CN ($J_K = 6_2$–5_2), (e) CH_3OH ($2_{1,2}$–$1_{1,1}$ A), (f) CH_3OH ($2_{-1,1}$–$1_{-1,0}$ E), and (g) CH_3CHO ($5_{0,5}$–$4_{0,4}$ E). Color scale and white contours show moment 0 maps of each line, and yellow contours are the continuum image (5σ, 10σ, 15σ, 150σ, 250σ, and 350σ). The rms noise (denoted as σ) and contour levels of each panel are as follows: (a) rms = 0.04 Jy beam^{-1} km s^{-1} (4σ, 5σ, 6σ, 7σ, and 8σ); (b) rms = 0.0043 Jy beam^{-1} km s^{-1} (3σ, 4σ, and 5σ); (c) rms = 0.0032 Jy beam^{-1} km s^{-1} (3σ, 4σ, 5σ, and 6σ); (d) rms = 0.005 Jy beam^{-1} km s^{-1} (3, 4σ, 5σ, and 6σ); (e) rms = 0.0077 Jy beam^{-1} km s^{-1} (5σ, 7σ, 9σ, 11σ, 13σ, and 15σ); (f) rms = 0.009 Jy beam^{-1} km s^{-1} (5σ, 7σ, 9σ, and 11σ); (g) rms = 0.0039 Jy beam^{-1} km s^{-1} (3σ, 4σ, and 5σ). Close-up images of each panel are shown below. These regions are indicated by a white dashed square in panel (a). Color scales are adjusted for the close-up ones. The black and white contours are the continuum map same as in the right panel of Figure 1.

Two spectral windows were set for CH_3CH_2CN ($12_{2,10} - 11_{2,9}$; $E_{up} = 38.2$ K) and CH_3OCHO ($8_{3,6} - 7_{3,5}$; $E_{up} = 27.3$ K). However, these lines of the large COMs were not detected with the current sensitivities. These two lines have low E_{up} values, and they should be easily detected if G28.28 is a COM-rich hot core. In fact, the similar E_{up} line of CH_3CH_2CN has been detected from the MYSOs studied by K. Taniguchi et al. (2023a). Their nondetection therefore suggests that G28.28 is deficient in large COMs; this point is quantified in Section 4.3.

Table 3
Properties of Positions for Molecular Line Analyses

Position	Coordinate[a] (R.A., Decl.)	Size [b] (arcsec × arcsec)	Flux [c] (mJy)	$N(H_2)$[d e], (cm^{-2})	$n(H_2)$[e], (cm^{-3})
G28.28	$18^h44^m13^s.278$, −4°18′04″.749	2.3 × 2.3	77 ± 17	(1.2 ± 0.3) × 10^{24}	(1.2 ± 0.2) × 10^7
Peak 1	$18^h44^m13^s.991$, −4°18′00″.392	3.5 × 2.6	6 ± 2	(1.4 ± 0.4) × 10^{23}	(1.1 ± 0.4) × 10^6
Peak 2	$18^h44^m14^s.169$, −4°18′05″.058	2.3 × 2.3	11 ± 2	(4.5 ± 0.9) × 10^{23}	(4.4 ± 0.9) × 10^6
Peak 3	$18^h44^m14^s.778$, −4°18′16″.900	2.3 × 2.3	5 ± 1	(2.2 ± 0.5) × 10^{23}	(2.1 ± 0.5) × 10^6
Peak 4	$18^h44^m14^s.501$, −4°18′09″.433	1.7 × 1.7	3 ± 2	(3.2 ± 1.9) × 10^{23}	(4.1 ± 2.5) × 10^6

Notes.
[a] J2000 coordinates.
[b] The major and minor axes of the chosen circle/elliptical aperture displayed in Figure 3.
[c] Flux values were measured in the continuum image.
[d] Assuming the optically thin dense gas case ($\beta = 1.5$; M. Bonfand et al. 2024). Details are described in Appendix B.
[e] The listed values are aperture-averaged values.

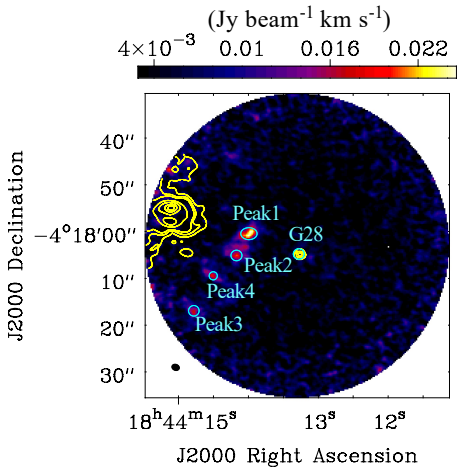

Figure 3. Positions selected for line analysis. Color scale indicates the moment 0 map of the HC_5N ($J = 36$–35) line, and the yellow contours show the continuum emission of 5σ, 10σ, 15σ, 50σ, 100σ, 200σ, and 300σ. Cyan circles/ellipses indicate the region for the spectral analysis.

3.2.2. Spectral Analyses with CASSIS

We selected positions to analyze molecular lines based on the moment 0 map of the HC_5N ($J = 36$–35) line. For G28.28, we double checked the moment 0 map of CH_3CN because it is a typical hot-core tracer. The aperture size of 2″.3 for G28.28 was chosen to cover molecular emission coming from the hot-core region. This aperture size corresponds to 0.03 pc at the source distance (3 kpc), and is hence reasonable for deriving the hot-core-averaged column densities. In addition to the MYSO G28.28, we identified four peaks between the MYSO G28.28 and the UCH II region, as shown in cyan circles/ellipses in Figure 3. We created the spectra by averaging the emission within these circles/ellipses. We named these peaks Peak 1–Peak 4, respectively. Table 3 summarizes the information on these positions. There are no clear continuum peaks at the positions of Peak 1–Peak 4 in Figure 1, but weak emission was detected. The continuum fluxes at Peak 1–Peak 4 are lower than that at the MYSO G28.28 by factors of 7–23. We calculated the H_2 column density and number density at each position using the 2.75 mm continuum data. The method to derive the column densities of H_2, $N(H_2)$ is explained in Appendix B. The values of $N(H_2)$ and $n(H_2)$ listed in Table 3 are the aperture-averaged values. When we applied the results of the 2D Gaussian fit for G28.28 (Table 2), $N(H_2)$, τ, and $n(H_2)$ are derived to be 3.3 × 10^{24} cm^{-2}, 0.058, and 5.3 × 10^7 cm^{-3}, respectively, that is, the obtained values change by only a factor of a few.

We analyzed molecular line data with the Markov Chain Monte Carlo (MCMC) method using the CASSIS software (C. Vastel et al. 2015). We assumed the local thermodynamic equilibrium (LTE) condition. This assumption is applicable because the gas densities at the five positions (Table 3) are comparable to the critical densities of the molecular lines (≈10^5–10^6 cm^{-3}). The line parameters used for the fitting are summarized in Table C1 in Appendix C. In the analyses, we fixed the emission size to the extraction region adopted for each position, as listed in Table 3. We conducted 2D Gaussian fitting for the G28.28 peak in all of the moment 0 maps, except for the HC_5N ($J = 36$–35) line, and confirmed that the emission regions of molecular lines are comparable to or larger than the chosen aperture size (2″.3). Regarding Peak 1–Peak 4 and the HC_5N ($J = 36$–35) line at G28.28, we confirmed that all of the molecular emission regions fill the beam sizes in their moment 0 maps. In the CASSIS software, the beam filling factor of $\theta^2_{\rm source}/(\theta^2_{\rm source} + \theta^2_{\rm beam})$ is applied. Here, $\theta_{\rm source}$ and $\theta_{\rm beam}$ are the source size and the synthesized beam, respectively. We fixed the source sizes at the aperture sizes for creating spectra listed in Table 3. The derived column densities should be regarded as aperture-averaged values.

We analyzed CH_3CN to obtain column densities and excitation temperatures from its K-ladder lines ($K = 0$–3). The excitation temperature derived from CH_3CN is a good thermometer for hot dense molecular cores (V. Hernández-Hernández et al. 2014; T. R. Hunter et al. 2014; K. Taniguchi et al. 2023b). Then, its excitation temperatures were applied to the other molecular analyses, except for CH_3OH. We derived column densities and excitation temperatures of CH_3OH by fitting its four lines. In the analysis of the CH_3OH lines, we excluded lines with non-Gaussian profiles from the fitting.

Figure 4 shows the spectra at the MYSO G28.28 as examples. The spectra at Peak 1–Peak 4 are presented in Figures C1 and C2 in Appendix C. The black and red lines indicate the observed spectra and the best-fitting model, respectively. We applied a two-velocity component fit, except for CH_3OH, at the MYSO G28.28. Table 4 summarizes the parameters obtained from the MCMC analysis. Since the HC_5N ($J = 37$–36) line shows an S/N lower than 4, we

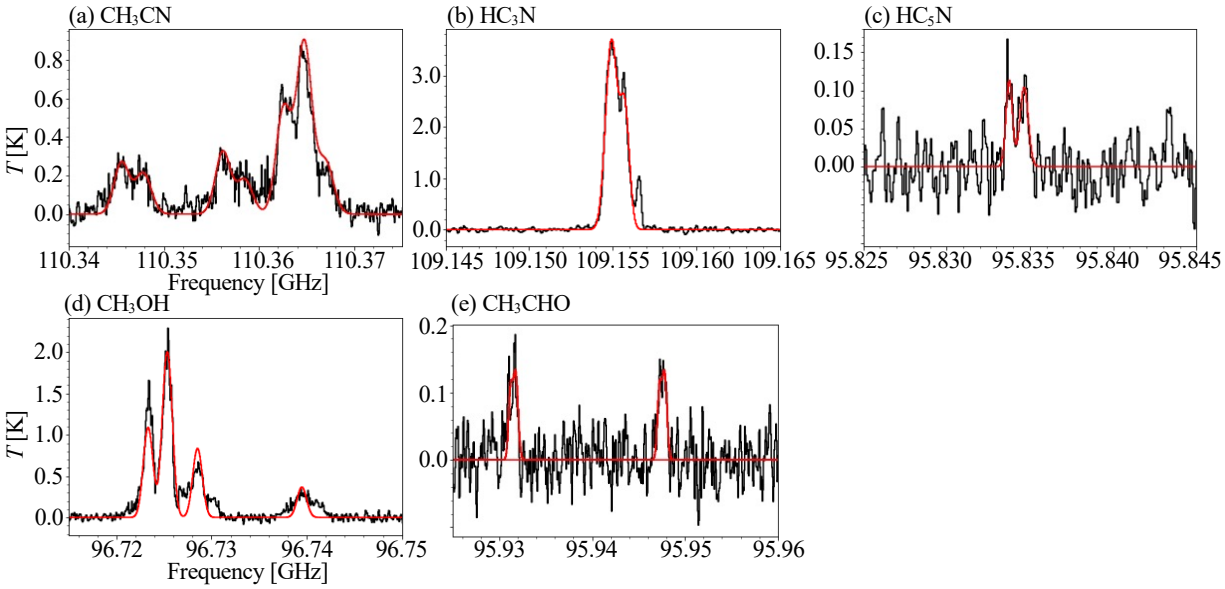

Figure 4. Spectra at the G28.28 continuum peak: (a) CH_3CN, (b) HC_3N, (c) HC_5N, (d) CH_3OH, and (e) CH_3CHO. Black and red lines indicate the observed spectra and the best-fitting models by CASSIS, respectively.

excluded it from the fitting. The optical depths of these molecular lines are small ($\tau \approx 0.003$–0.05).

We conducted additional tests by changing emission (source) sizes to investigate how much the derived column densities are affected by uncertainties in emission sizes (i.e., beam filling factors). We changed the emission size from the aperture size (Table 3) to 1.″3 (the synthesized beam size). Even if the emission size was reduced, all of the molecular lines remained optically thin ($\tau \ll 0.1$), and the column densities increased by less than a factor of 2. Hence, the aperture-averaged column densities were not significantly affected by uncertainties in the beam filling factor.

The excitation temperature derived toward the MYSO G28.28 is 100 K, whereas those derived at Peak 1–Peak 4 show much lower values (25–30 K). The line widths at the MYSO G28.28 are wider than those at the other positions. These results indicate that the MYSO G28.28 harbors hotter gas compared to the other positions.

4. Discussion

4.1. Properties of the Cyanopolyyne Emission Regions between the MYSO G28.28 and the UCH II Region

We found strong emission regions of cyanopolyynes (HC_3N and HC_5N) between the MYSO G28.28 and the UCH II region, i.e., Peak 1–Peak 4 (Figure 3). We discuss properties of these regions and the origin of the cyanopolyyne emission in this subsection.

These emission regions were also detected in the VLA Ka-band observations (K. Taniguchi et al. 2018a). In the VLA observations, only the low-E_{up} lines were covered: 4.4 K and 13.4 K for HC_3N and HC_5N, respectively. These lines have low critical densities ($\approx 10^4$ cm^{-3}). They spatially correlate with the 450 μm continuum emission. K. Taniguchi et al. (2018a) proposed that these regions harbor low-mass or intermediate-mass protostellar cores and that the WCCC mechanism works.

We found that the 2.75 mm continuum fluxes at the HC_5N peak positions are weaker than that at the MYSO G28.28 (Table 3), which supports that these positions do not contain high-mass protostellar cores. The derived $n(H_2)$ values at Peak 1–Peak 4 are higher than 10^6 cm^{-3} (Table 3), indicating dense gas. As we point out in Appendix B, our assumption that the length of the core is equal to the beam size could overestimate $n(H_2)$ at these four positions. However, the detection of the lines with high critical densities (10^5–10^6 cm^{-3}) supports that the gas densities at Peak 1–Peak 4 are at least moderate values ($\sim 10^5$ cm^{-3}). Together with the detection of high-E_{up} HC_5N lines, this suggests that these peaks trace moderately dense and warm regions. They may be associated with low- or intermediate-mass protostellar cores, although the current data do not prove the presence of embedded protostars.

The derived excitation temperatures of CH_3CN at Peak 1–Peak 4 are $\sim$25–30 K (Table 4), corresponding to the temperature at which the WCCC mechanism works efficiently. Thus, the observed temperatures are consistent with conditions under which WCCC-like chemistry can enhance HC_5N.

We consider the possibility of external heating from the nearby UCH II region, which could contribute to exciting the high-J lines. The external UV radiation could be shielded at the central cores of Peak 1–Peak 4, where the H_2 number densities are on the order of 10^6 cm^{-3} (M. Juvela & N. Ysard 2011). However, the penetration of the UV radiation strongly depends on the density structure of molecular clouds. Thus, with the current datasets, we cannot completely exclude a contribution from external heating by the nearby UCH II region.

4.2. Comparison of Chemical Compositions among the Five Representative Positions

We compare the chemical compositions among the five positions (G28.28 and Peak 1–Peak 4) in this subsection. We calculate and compare the column density ratios of $[X]/[CH_3CN]$, where X represents molecular species except for CH_3CN. Since CH_3CN has been detected at all of the positions and its column densities are the most reliable due to its four-line fitting, we chose this species as the reference. The beam filling factor does not affect the molecular emission

Table 4
Results of the Spectral Analyses

Species	N (cm^{-2})	T_{ex} (K)	FWHM [a] (km s^{-1})	V_{LSR} (km s^{-1})
G 28 (1st Component)				
HC_3N	$(6.21 \pm 0.05) \times 10^{13}$	50.2 (fixed)	2.23 ± 0.17	51.34 ± 0.17
HC_5N	$(3.4 \pm 0.5) \times 10^{12}$	50.2 (fixed)	1.44 ± 0.22	51.84 ± 0.17
CH_3CN	$(4.8 \pm 0.1) \times 10^{13}$	50.2 ± 0.3	5.32 ± 0.27	50.97 ± 0.18
CH_3OH	$(1.17 \pm 0.2) \times 10^{15}$	13.2 ± 0.3	3.59 ± 0.17	49.60 ± 0.17
CH_3CHO	$(4.0 \pm 0.4) \times 10^{13}$	50.2 (fixed)	1.50 ± 0.18	50.65 ± 0.18
G 28 (2nd Component)				
HC_3N	$(4.0 \pm 0.1) \times 10^{13}$	100.5 (fixed)	1.69 ± 0.18	49.16 ± 0.17
HC_5N	$(3.1 \pm 0.4) \times 10^{12}$	100.5 (fixed)	1.62 ± 0.24	48.97 ± 0.17
CH_3CN	$(4.5 \pm 0.2) \times 10^{13}$	100.5 ± 0.3	5.13 ± 0.27	44.8 ± 0.2
CH_3OH	...	...	...	...
CH_3CHO	$(1.7 \pm 0.1) \times 10^{14}$	100.5 (fixed)	1.89 ± 0.18	49.0 ± 0.2
Peak 1				
HC_3N	$(8.82 \pm 0.03) \times 10^{13}$	30.1 (fixed)	1.07 ± 0.17	49.42 ± 0.17
HC_5N	$(3.92 \pm 0.09) \times 10^{13}$	30.1 (fixed)	1.00 ± 0.17	49.50 ± 0.17
CH_3CN	$(9.3 \pm 0.2) \times 10^{12}$	30.1 ± 0.1	1.08 ± 0.17	49.43 ± 0.17
CH_3OH	$(2.95 \pm 0.06) \times 10^{14}$	9.6 ± 0.3	1.80 ± 0.17	49.04 ± 0.17
CH_3CHO	$(2.5 \pm 0.1) \times 10^{13}$	30.1 (fixed)	1.39 ± 0.17	49.51 ± 0.17
Peak 2				
HC_3N	$(1.12 \pm 0.01) \times 10^{14}$	30 (fixed)	1.49 ± 0.17	49.32 ± 0.17
HC_5N	$(2.6 \pm 0.1) \times 10^{13}$	30 (fixed)	1.00 ± 0.17	49.27 ± 0.17
CH_3CN	$(1.40 \pm 0.02) \times 10^{13}$	30.04 ± 0.03	1.42 ± 0.17	49.24 ± 0.17
CH_3OH	$(1.27 \pm 0.01) \times 10^{15}$	10.6 ± 0.1	1.41 ± 0.17	49.02 ± 0.17
CH_3CHO	$(3.2 \pm 0.3) \times 10^{13}$	30 (fixed)	2.2 ± 0.4	49.45 ± 0.18
Peak 3				
HC_3N	$(6.39 \pm 0.02) \times 10^{13}$	30.1 (fixed)	1.06 ± 0.17	46.23 ± 0.17
HC_5N	$(2.47 \pm 0.09) \times 10^{13}$	30.1 (fixed)	1.50 ± 0.17	46.28 ± 0.17
CH_3CN	$(7.0 \pm 0.3) \times 10^{12}$	30.13 ± 0.04	1.44 ± 0.17	46.39 ± 0.17
CH_3OH	$(8.3 \pm 0.7) \times 10^{14}$	16.1 ± 0.7	3.4 ± 0.3	46.88 ± 0.17
CH_3CHO	$(3.0 \pm 0.3) \times 10^{13}$	30.1 (fixed)	1.54 ± 0.18	46.69 ± 0.18
Peak 4				
HC_3N	$(3.99 \pm 0.02) \times 10^{13}$	24.9 (fixed)	0.61 ± 0.17	50.24 ± 0.17
HC_5N	$(4.10 \pm 0.09) \times 10^{13}$	24.9 (fixed)	0.59 ± 0.17	50.36 ± 0.17
CH_3CN	$(2.5 \pm 0.5) \times 10^{12}$	24.9 ± 0.1	0.42 ± 0.17	50.34 ± 0.17
CH_3OH	$(2.17 \pm 0.04) \times 10^{14}$	10.2 ± 0.1	2.30 ± 0.17	49.10 ± 0.17
CH_3CHO	...	...	...	...

Note.
[a] Errors include the system uncertainties originating from the velocity resolution of the spectral window setup (0.168 km s^{-1}).

ratios if the emission comes from similar regions and their lines are optically thin. In Section 3.2, we confirmed that all of the molecular lines are optically thin even if the emission size is smaller than the applied aperture sizes. Thus, the aperture-averaged column densities can be used for this comparison. We exclude CH_3CHO because of large uncertainties in emission sizes. Moreover, unlike the cyanopolyynes, the detected CH_3CHO lines have a low upper-state energy (E_{up} = 13.9 K), and their emission may contain contributions from the outer envelopes. Hence, the emission regions of the CH_3CHO lines could differ from those of the CH_3CN lines that predominantly trace the hot-core region. Figure 5 shows the column density ratios with respect to CH_3CN among the five positions. Note that the fitting result of the CH_3OH spectra at Peak 3 is tentative and its accuracy is low. We exclude it from the detailed discussion.

The column density ratios of HC_3N/CH_3CN and HC_5N/CH_3CN at G28.28 are ∼0.9–1.3 and ∼0.07, respectively. We compared the column density ratio of HC_5N/CH_3CN at G28.28 to the chemical network simulations presented by K. Taniguchi et al. (2023a). We found that the observed ratio agrees with the model when the temperature reaches the sublimation temperatures of HC_5N and CH_3CN. Hence, HC_5N is formed via the HCCC mechanism at G28.28. This is consistent with the derived excitation temperatures of CH_3CN (100.5 K; Table 4).

The ratios of HC_3N/CH_3CN and HC_5N/CH_3CN at the four HC_5N peak positions (Peak 1–Peak 4) are ∼8–16 and 2–16, respectively. Thus, cyanopolyynes at the MYSO G28.28 show lower ratios compared to the HC_5N peak positions by more than 1 order of magnitude, which means that their chemistry at G28.28 differs from that at Peak 1–Peak 4. We found smaller differences in the HC_3N/CH_3CN ratio among Peak 1–Peak 4 compared to HC_5N. This may be because the HC_3N emission is contaminated by outer envelopes, given that the observed HC_3N line has a moderate E_{up} value (34.1 K) compared to HC_5N (85.1 K). The chemical composition of the natal molecular cloud could affect the column density ratio of HC_3N/CH_3CN.

Methanol (CH_3OH) shows lower T_{ex} values compared to CH_3CN (Table 4). This implies that the CH_3OH emission comes not only from hot-core regions but also from outer

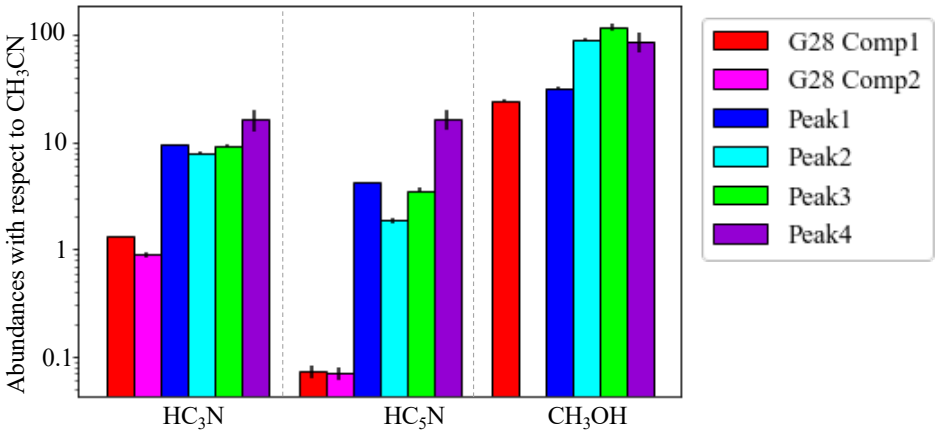

Figure 5. Comparisons of column density ratios with respect to CH_3CN at the five positions. The error bars indicate the standard deviation.

envelopes. The CH_3OH lines show a non-Gaussian profile at G28.28 (Figure 4), suggesting contamination from molecular outflows and/or outer envelopes or molecular clouds. Thus, the detected lines of CH_3OH may be contaminated by outer envelopes or natal clouds rather than central hot gas. This contamination may explain why the CH_3OH/CH_3CN ratios do not differ strongly among the five positions.

4.3. Comparisons of Chemical Compositions between the MYSO G28.28 and Other MYSOs

K. Taniguchi et al. (2023a) analyzed ALMA Band 3 data toward five MYSOs, and derived the abundances with respect to CH_3CN (see Figure 14 in their paper). They reported that the HC_5N ($J = 35$–34, $E_{up} = 80.5$ K) line is detected from four cores, and it is always associated with large COMs, which means that HC_5N has been detected from chemically rich hot cores. In this subsection, we compare the chemical compositions of the MYSO G28.28 to those presented by K. Taniguchi et al. (2023a).

The derived HC_5N/CH_3CN ratios at G28.28 are ≈0.07. The HC_5N/CH_3CN ratios in the four sources investigated by K. Taniguchi et al. (2023a) are ≈0.001–0.04. Thus, the ratios at G28.28 are higher by factors of ∼2–70, suggesting that G28.28 is the most cyanopolyyne-rich MYSO.

The CH_3OH/CH_3CN ratio at G28.28 is 24.7, whereas the ratios in the MYSOs studied by K. Taniguchi et al. (2023a) are 7–1300. Note that K. Taniguchi et al. (2023a) derived the column density of CH_3OH using its vibrationally excited line with a high E_{up} (302.9 K) with an assumption that its excitation temperatures are equal to those of CH_3CN. This CH_3OH line traces only inner hot-core regions. On the other hand, the CH_3OH lines in the present work are likely contaminated by outer envelopes (Section 4.2). Thus, the comparisons of the CH_3OH/CH_3CN ratio may be misleading. If the CH_3OH column densities derived by K. Taniguchi et al. (2023a) trace only hot-core components, those values would be lower limits to the total CH_3OH column densities. If the outer components of CH_3OH, which are similar to those traced in our observations, are included, the column densities of CH_3OH could be higher. Thus, it can be said that CH_3OH is deficient at G28.28, especially in the hot region (>100 K), compared to COM-rich hot cores.

Here, we highlight that large COMs are especially deficient in G28.28. We could not detect CH_3CH_2CN ($12_{2,10}$–$11_{2,9}$; $E_{up} = 38.2$ K) and CH_3OCHO ($8_{3,6} - 7_{3,5}$; $E_{up} = 27.3$ K) lines. The previously studied MYSOs associated with HC_5N were found to be COM rich; both nitrogen (N)-bearing and oxygen (O)-bearing COMs are abundant. This is clearly different from G28.28. Quantitative investigation with their upper limits will be discussed in Section 4.4.

In summary, G28.28 has unique chemical features; cyanopolyynes are abundant, whereas COMs are deficient. These features are the same as the low-mass WCCC source L1527 (N. Sakai & S. Yamamoto 2013).

4.4. The Unique Chemical Features of the MYSO G28.28

K. Taniguchi et al. (2023a) mentioned that HC_5N and large N-bearing COMs (CH_2CHCN and CH_3CH_2CN) are always detected together. On the other hand, we could not detect large COMs (CH_3OCHO and CH_3CH_2CN) from G28.28, as we discussed in Section 4.3. We derived upper limits for their column densities: 3.0×10^{14} cm^{-2} for CH_3OCHO and 1.2×10^{13} cm^{-2} for CH_3CH_2CN, respectively. These correspond to fractional abundances with respect to H_2 of 2.5×10^{-10} and 1.0×10^{-11}, respectively. These abundances are lower than those in other hot cores by more than 1 order of magnitude (Y. Peng et al. 2022; C. Li et al. 2024).

The upper limit of the column density ratio of CH_3CH_2CN/CH_3CN at G28.28 is 0.13. The MYSOs studied by K. Taniguchi et al. (2023a) show CH_3CH_2CN/CH_3CN column density ratios of 0.11–0.58. Figure 6 shows comparisons of the column density ratios of HC_5N/CH_3CN versus CH_3CH_2CN/CH_3CN among G28.28 and the MYSOs studied by K. Taniguchi et al. (2023a). The previously studied MYSOs are divided into two groups: both ratios are high (G9C2 and G10) or low (G9C3 and G12). G28.28 is distinct from these two groups, showing a higher HC_5N/CH_3CN ratio in comparison to the other MYSOs. On the other hand, the upper limit of the CH_3CH_2CN/CH_3CN ratio is lower than those in G9C2 and G10 by a factor of ∼4–4.5. G12 and G9C3 show similar CH_3CH_2CN/CH_3CN ratios with the upper limit at G28.28, but their HC_5N/CH_3CN ratios are lower than that at G28.28 by a factor of ∼43–50. Even if we consider the different sensitivities and beam sizes among our observations and the previous study, the differences in the column density ratios would be less than 1 order of magnitude. Thus, G28.28 is genuinely deficient in COMs, making its chemical

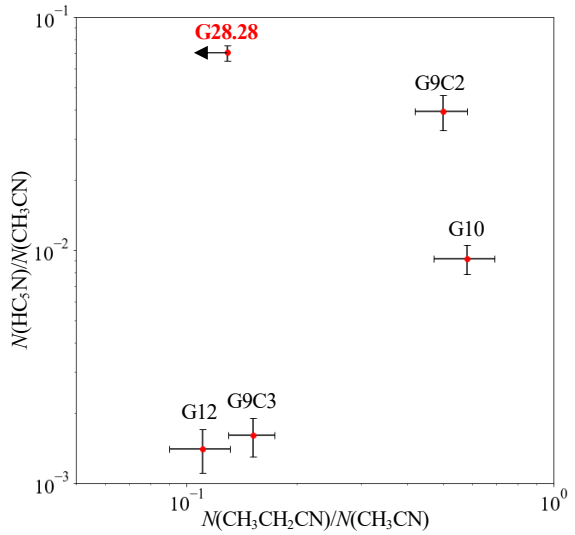

Figure 6. Comparison of column density ratios of HC_5N/CH_3CN versus CH_3CH_2CN/CH_3CN among G28.28 and the previously studied MYSOs by K. Taniguchi et al. (2023a). The error bars indicate the standard deviation.

composition different from those of the other MYSOs studied by K. Taniguchi et al. (2023a).

Although G28.28 contains hot gas with temperatures above 100 K, where ice mantles sublimate, COMs are significantly deficient. This indicates that the COM-poor nature of G28.28 is not simply due to low temperature. In our ALMA observations, the frequency coverage is limited. We then checked the previous single-dish observations covering a wide frequency range (K. Taniguchi et al. 2018c). They detected only two COMs, CH_3OH and CH_3CHO, whereas many lines of COMs have been detected from the other two MYSOs (see Table 6 of K. Taniguchi et al. 2018c).

In summary, the unique chemical features of G28.28 are that (1) the HCCC mechanism produces HC_5N in the hot region with temperatures above 100 K, and (2) COMs are deficient even though G28.28 harbors a hot region. To the best of our knowledge, G28.28 is the first HCCC source, in the categorization of the chemical diversity around protostars proposed by K. Taniguchi et al. (2024a).

5. Conclusion

We have presented ALMA Band 3 data toward the MYSO G28.28. Both cyanopolyynes (HC_3N and HC_5N) and COMs (CH_3OH, CH_3CN, and CH_3CHO) have been detected. On the other hand, large COMs (CH_3CH_2CN and CH_3OCHO) were not detected. The main conclusions of this paper are as follows:

1. The detected HC_5N and CH_3CN lines from G28.28 trace a hot-core region with temperatures above 100 K. These results indicate that HC_5N forms by the HCCC mechanism.
2. Additional HC_5N peak positions have been identified between the MYSO G28.28 and the nearby UCH II region. Their densities and excitation temperatures are consistent with dense, moderately warm gas, possibly associated with low- or intermediate-mass protostellar cores. The chemistry at these positions may be related to WCCC-like carbon-chain formation, although external heating from the nearby UCH II region cannot be excluded with the present data.
3. The high-sensitivity, high-angular resolution ALMA Band 3 data confirm that G28.28 is cyanopolyyne rich but COM poor. Such a chemical feature is different from the MYSOs previously studied with ALMA Band 3 (K. Taniguchi et al. 2023a).

We found that G28.28 is the counterpart of the low-mass WCCC source L1527. The MYSO G28.28 is the first HCCC source: a cyanopolyyne-rich but COM-poor high-mass protostellar core harboring a hot region ($T > 100$ K).

Understanding the origin(s) of this chemical diversity will be key to improving our understanding of the star formation process, including the role of natal environments. These points will be studied with large samples located in various environments.

Most chemical network simulations show that the most efficient formation route of cyanopolyynes is the reaction of "$C_{2n}H_2 + CN$" during the warm-up stage (J. F. Chapman et al. 2009; K. Taniguchi et al. 2019a), and this reaction is proposed as the most promising formation pathway of cyanopolyynes in the HCCC mechanism at present. However, it is difficult to directly prove it by observations. One method to investigate the formation process of long cyanopolyynes is observing ^{13}C isotopologues (K. Taniguchi et al. 2016a; A. M. Burkhardt et al. 2018). Such observations are currently difficult even with ALMA due to the required long integration times because we need to detect the ^{13}C isotopologues with $S/N > 10$. Although the concentration of ^{13}C in CN may not be efficient in the warm gas, K. Taniguchi et al. (2016b) demonstrated that this method can be applied to HC_3N in the warm gas around both low-mass and high-mass protostars. Observations with future facilities are necessary for direct evidence of the HCCC mechanism.

Acknowledgments

This paper makes use of the following ALMA data: ADS/JAO. ALMA#2023.1.00467.S. ALMA is a partnership of ESO (representing its member states), NSF (USA), and NINS (Japan), together with NRC (Canada), NSTC and ASIAA (Taiwan), and KASI (Republic of Korea), in cooperation with the Republic of Chile. The Joint ALMA Observatory is operated by ESO, AUI/NRAO, and NAOJ. Data analysis was in part carried out on the Multi-wavelength Data Analysis System operated by the Astronomy Data Center (ADC), National Astronomical Observatory of Japan.

K.T. is supported by JSPS KAKENHI grant Nos. 21H01142, 24K17096, and 24H00252. K.T. was supported by the ALMA Japan Research Grant of NAOJ ALMA Project, NAOJ-ALMA-410. O.S. acknowledges the financial support of the Max Planck Society. T.S. acknowledges the financial support of the Yamada Science Foundation. We also thank the anonymous referee for the valuable feedback that has improved the quality of this work.

Facility: Atacama Large Millimeter/submillimeter Array (ALMA).

Software: CASA (CASA Team et al. 2022), CASSIS (C. Vastel et al. 2015),

Appendix A
SED Fitting of Infrared Data

For the SED fitting, we used archival data from Spitzer/IRAC (M. W. Werner et al. 2004; G. G. Fazio et al. 2004) at 3.6, 4.5, 5.8, and 8.0 μm obtained from the Spitzer Heritage Archive, along with Herschel/PACS and SPIRE (M. J. Griffin et al. 2010) data at 70, 160, 250, 350, and 500 μm from the ESA Herschel Science Archive. In addition, Spitzer/MIPS 24 μm data were included. The Herschel 70 μm image was used to automatically determine the optimal aperture using specialized functions from `sedcreator` (R. Fedriani et al. 2023), yielding an aperture of 25″ (radius). This aperture was then adopted as a fixed aperture to extract fluxes at all wavelengths. Background subtraction was performed using an annulus with an inner radius equal to the aperture radius and an outer radius of twice the aperture radius. Figure A1 presents the resulting SED fit, and Figure A2 shows the corresponding two-dimensional parameter space of the model fits. The best-fit SED parameters are summarized in Table A1. The reported model parameters and derived quantities include the χ^2 goodness-of-fit statistic; M_c, the core mass; $\Sigma_{\rm cl}$, the mass surface density of the surrounding clump; R_c, the core radius; m_*, the stellar mass; $\theta_{\rm view}$, the viewing angle measured from the outflow axis; A_V, the line-of-sight visual extinction; $M_{\rm env}$, the envelope mass; $\theta_{\rm w,esc}$, the half-opening angle of the outflow cavity (escape angle); $\dot{M}_{\rm disk}$, the disk accretion rate onto the star; $L_{\rm bol,iso}$, the isotropic bolometric luminosity; and $L_{\rm bol}$, the true bolometric luminosity of the source.

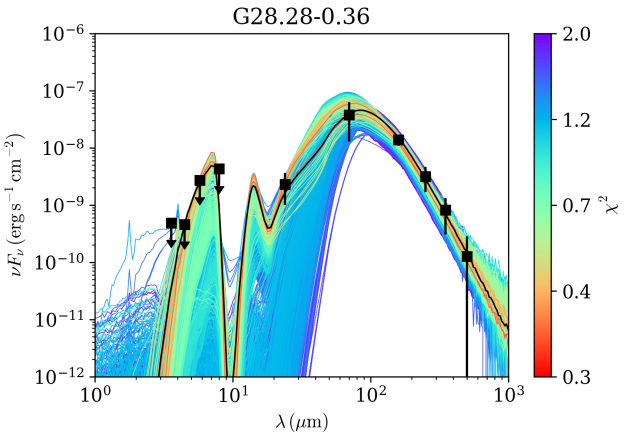

Figure A1. SED fitting of the MYSO G28.28. The fixed-aperture, background-subtracted SED was fitted using the protostellar model grid (Y. Zhang & J. C. Tan 2018). The best-fitting model is shown by the black line, while all other "good models" are displayed by colored lines, ranging from red to blue with increasing χ^2. We define "good" models depending on the minimum value of χ^2, *i. e.* , $\chi^2_{\rm min}$ (see R. Fedriani et al. 2023; Z. Telkamp et al. 2025).

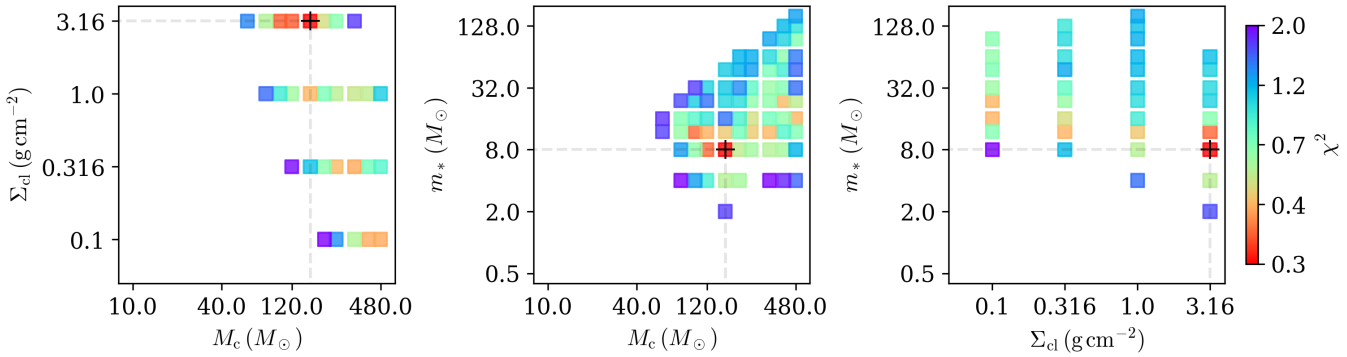

Figure A2. Comparison of key model parameters for source G28.28-0.36. The panels show $\Sigma_{\rm cl}$ versus M_c (left column), m_* versus M_c (center column), and m_* versus $\Sigma_{\rm cl}$ (right column) for "good" model fits, color-coded by their χ^2 values. The black cross indicates the best-fitting model.

Table A1
Selected SED Model Parameters

χ^2	M_c ($M_\odot$)	$\Sigma_{\rm cl}$ (g cm^{-2})	R_c (pc)	m_* ($M_\odot$)	$\theta_{\rm view}$ (deg)	A_V (mag)	$M_{\rm env}$ ($M_\odot$)	$\theta_{\rm w,esc}$ (deg)	$\dot{M}_{\rm disk}$ ($\times10^{-4}M_\odot$ yr^{-1})	$L_{\rm bol,iso}$ ($\times10^4L_\odot$)	$L_{\rm bol}$ ($\times10^4L_\odot$)
0.18510	160.0	3.16	0.052362	8.0	12.83857	201.35329	145.8153	12.7017	8.51410	9.70607	2.00533
0.26705	120.0	3.16	0.045347	8.0	12.83857	214.48997	105.9249	14.9547	7.89885	11.8794	1.89690
0.23528	100.0	3.16	0.041396	12.0	12.83857	279.24634	76.72601	20.2152	9.39717	41.1093	5.24975
0.28694	120.0	3.16	0.045347	12.0	12.83857	281.13601	98.53957	17.8019	9.63771	41.7014	5.17369
0.25148	480.0	0.1	0.50982	16.0	12.83857	234.00543	440.0145	15.4996	1.19434	18.6013	3.85823
Average model[a]	196^{+284}_{-96}	$2.5^{+0.6}_{-2.4}$	$0.14^{+0.37}_{-0.10}$	$11.2^{+4.8}_{-3.2}$	12.83857	242^{+39}_{-41}	173^{+267}_{-97}	16 ± 4	$7.3^{+2.3}_{-6.1}$	$24.6^{+17.1}_{-14.9}$	$3.6^{+1.6}_{-1.7}$

Note.
[a] This corresponds to the average values of the above five good models. Upper and lower scripts in the average model row refer to the upper and lower range of the dispersion of the good models.

Appendix B
Calculation of $N(H_2)$

We calculated the dust opacity at G28.28 and Peak 1–Peak 4 using the following Equation (B1):

$$\tau = -\ln\left(1 - \frac{F_{2.75\mathrm{mm}}}{B_{2.75\mathrm{mm}}(T_{\mathrm{dust}})\Omega}\right), \quad \text{(B1)}$$

where $F_{2.75\mathrm{mm}}$, $B_{2.75\mathrm{mm}}(T_{\mathrm{dust}})$, and Ω are flux density integrated over the apertures listed in Table 3, the Planck function at 2.75 mm with a dust temperature of T_{dust}, and the solid angle of the aperture, respectively. We assumed that the dust temperature is equal to the excitation temperature of CH_3CN (K. Taniguchi et al. 2023b). Since we applied two-velocity component fitting to the MYSO G28.28, we used their average temperature (75.4 K) as the dust temperature. The obtained dust opacity values are 0.001–0.007 at all positions. Thus, the dust continuum emission at this frequency is optically thin in our target positions.

We derived the column density of H_2, $N(H_2)$, from the dust continuum data at 2.75 mm using the following Equation (B2):

$$N(\mathrm{H_2}) = \frac{F_{2.75\mathrm{mm}}\gamma}{B_{2.75\mathrm{mm}}(T_{\mathrm{dust}})\Omega\kappa_{2.75\mathrm{mm}}\mu_{\mathrm{H_2}}m_{\mathrm{H}}}, \quad \text{(B2)}$$

where $F_{2.75\mathrm{mm}}$, γ, $B_{2.75\mathrm{mm}}(T_{\mathrm{dust}})$, Ω, $\kappa_{2.75\mathrm{mm}}$, $\mu_{\mathrm{H_2}}$, and m_{H} are continuum flux density at 2.75 mm, gas-to-dust mass ratio, the Planck function at 2.75 mm with a dust temperature of T_{dust}, the solid angle of the aperture, the dust mass opacity, the H_2 mean molecular weight (2.8), and the mass of the hydrogen atom, respectively.

The gas-to-dust ratio was derived using the following Equation (B3) (A. Giannetti et al. 2017):

$$\log(\gamma) = 0.087D_{\mathrm{GC}} + 1.44, \quad \text{(B3)}$$

where D_{GC} represents the distance from the Galactic Center. The D_{GC} value for G28.28 was calculated at 5.5 kpc (K. Taniguchi et al. 2021). The calculated dust-to-gas ratio is 83.

The $\kappa_{2.75\mathrm{mm}}$ value was calculated with the following Equation (B4):

$$\kappa_{2.75\mathrm{mm}} = \kappa_{1.3\mathrm{mm}}\left(\frac{\nu_{2.75\mathrm{mm}}}{\nu_{1.3\mathrm{mm}}}\right)^{\beta}, \quad \text{(B4)}$$

where $\kappa_{1.3\mathrm{mm}}$ is the dust mass opacity at 1.3 mm and $\beta = \alpha - 2$ (S. Terebey et al. 1993). The $\kappa_{1.3\mathrm{mm}}$ value of 0.9 $\mathrm{cm^2\,g^{-1}}$ (V. Ossenkopf & T. Henning 1994; K. Taniguchi et al. 2023b) was applied. We assumed that the dust emissivity (β) is equal to 1.5 here. K. Taniguchi et al. (2023a) derived the β values of 1.5–1.75 at the five MYSOs with similar ages using multiband infrared data. In addition, M. Bonfand et al. (2024) derived the H_2 column densities for hot cores with an assumption of $\beta = 1.5$. Thus, we considered that $\beta = 1.5$ can be applied to G28.28. The H_2 density values, $n(H_2)$, summarized in Table 3 were calculated with the assumption that the size along the line of sight of the core is equal to the aperture sizes listed in Table 3. This assumption is reasonable for G28.28, showing a centrally peaked feature. On the other hand, this assumption may not be applicable to Peak 1–Peak 4, because there is no centrally peaked feature and hence the determination of the appropriate line-of-sight scale is not straightforward. If the line-of-sight scale is underestimated, the derived $n(H_2)$ would be upper limits. Even if the line-of-sight scale is several factors larger than assumed here, the H_2 density is still higher than 10^5 $\mathrm{cm^{-3}}$. Thus, our assumption of the LTE condition in the molecular line analyses is reasonable.

Appendix C
Spectra at the Four HC_5N Peaks

Table C1 summarizes line parameters used in the MCMC fitting. Figures C1 and C2 show spectra at the four HC_5N peak positions (Peak 1–Peak 4), overlaid with the best-fitting models derived in the CASSIS software. The CH_3OH lines at Peak 3 could not be fitted even with two velocity components. The fitting results are tentative and shown by the dotted lines. No CH_3CHO line was detected at Peak 4.

Table C1
Line Parameters Used for the MCMC Fitting

Species	Transition	Frequency[a] (GHz)	E_{up} (K)
CH_3CN	6_3–5_3	110.36435	82.8
CH_3CN	6_2–5_2	110.37499	47.1
CH_3CN	6_1–5_1	110.38137	25.7
CH_3CN	6_0–5_0	110.38350	18.5
HC_3N	12–11	109.17363	34.1
HC_5N	36–35	95.850335	85.1
CH_3OH	$2_{1,2}$–$1_{1,1}$ E	96.739358	12.5
CH_3OH	$2_{0,2}$–$1_{0,1}$ A	96.741371	7.0
CH_3OH	$2_{-0,2}$–$1_{-0,1}$ E	96.744545	20.1
CH_3OH	$2_{-1,1}$–$1_{-1,0}$ E	96.755501	28.0
CH_3CHO	$5_{0,5}$–$4_{0,4}$ E	95.9474373	13.9
CH_3CHO	$5_{0,5}$–$4_{0,4}$ A	95.9634588	13.9

Note.
[a] Rest frequencies are taken from the Cologne Database for Molecular Spectroscopy (CDMS; C. P. Endres et al. (2016)) except for CH_3CHO, whose frequencies are taken from the JPL catalog (H. M. Pickett et al. 1998).

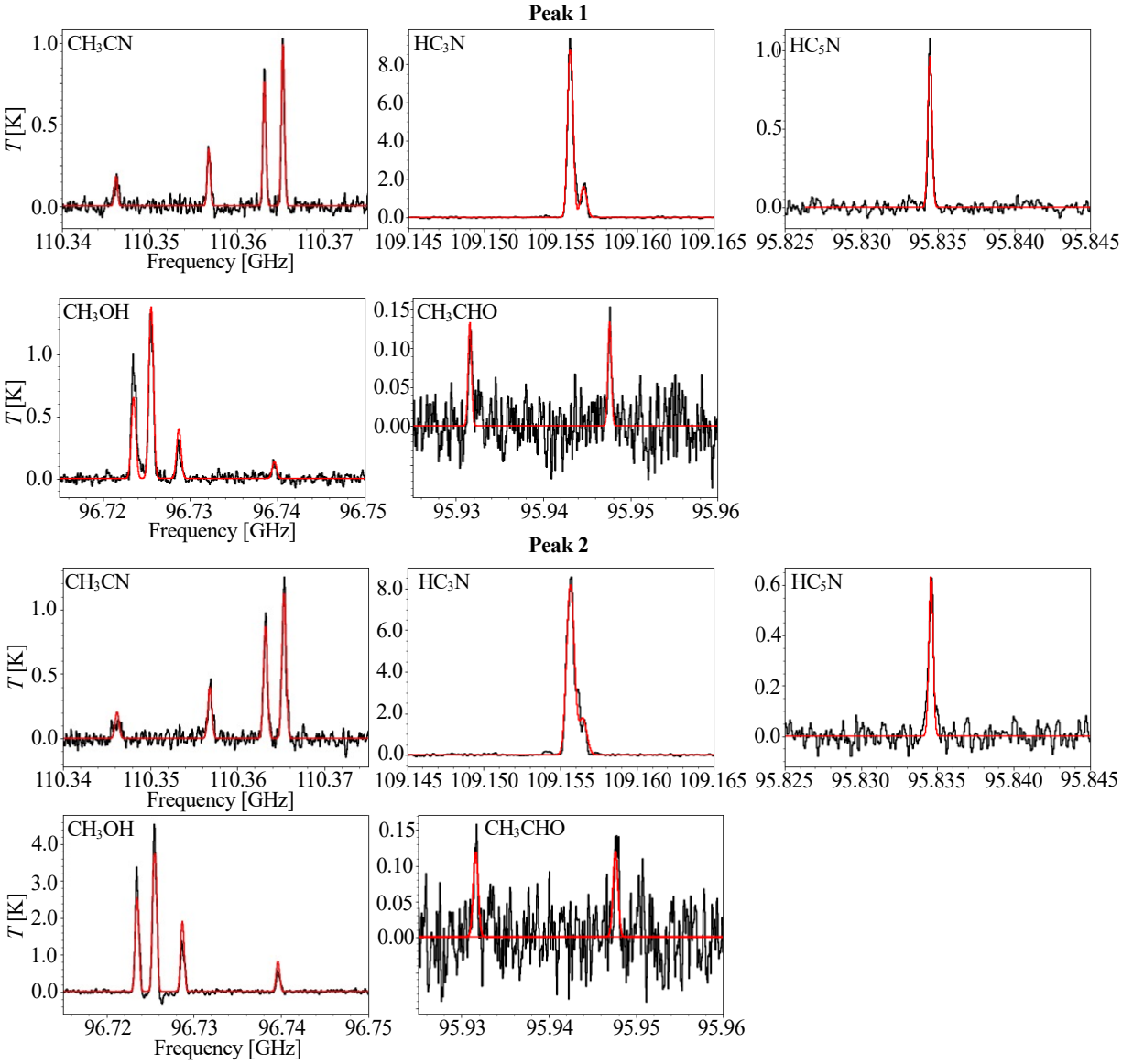

Figure C1. Spectra at Peak 1 (upper panels) and Peak 2 (lower panels). Black and red lines indicate the observed spectra and the best-fitting models by CASSIS, respectively.

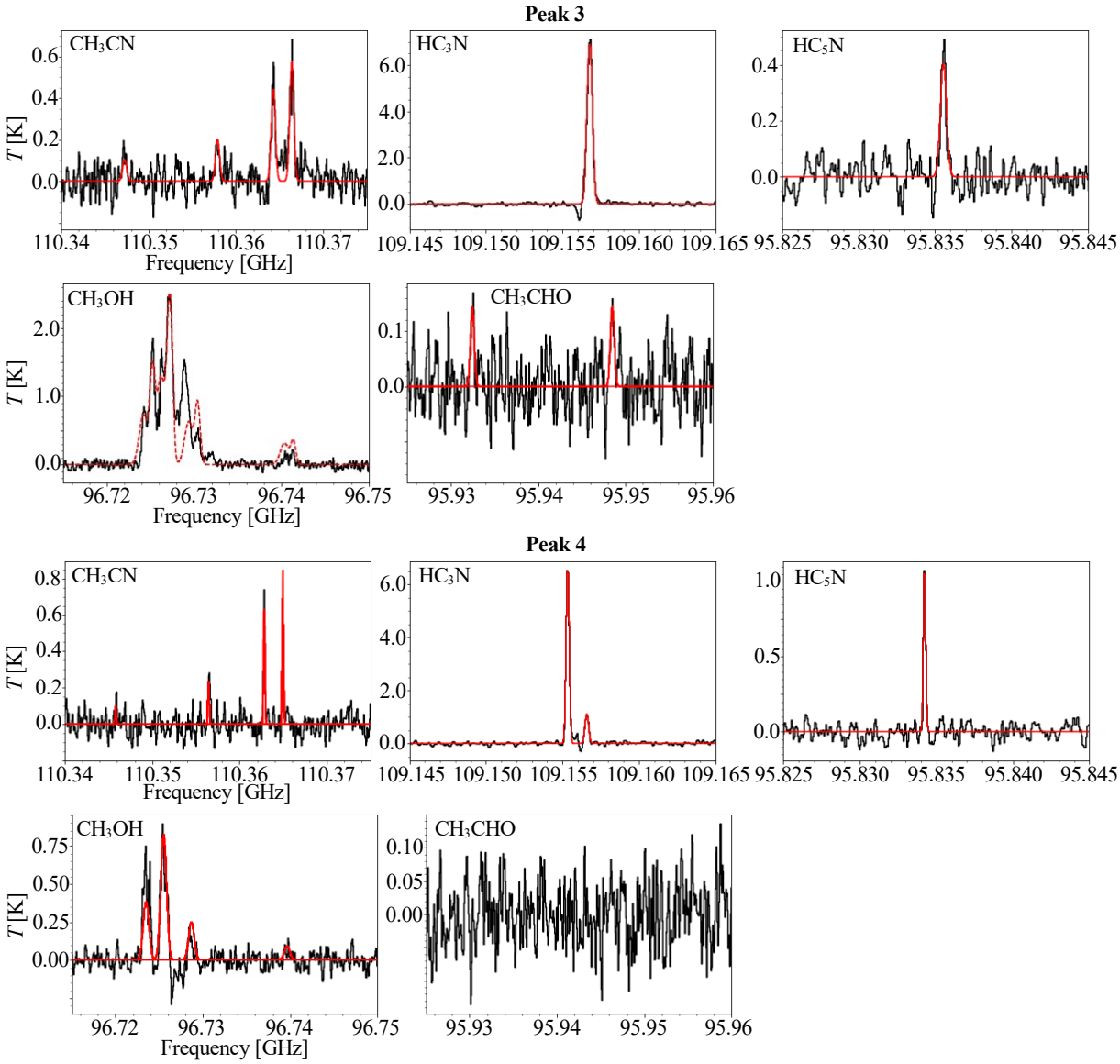

Figure C2. Spectra at Peak 3 (upper panels) and Peak 4 (lower panels). Black and red lines indicate the observed spectra and the best-fitting models by CASSIS, respectively.

ORCID iDs

Kotomi Taniguchi https://orcid.org/0000-0003-4402-6475
Masao Saito https://orcid.org/0000-0003-0769-8627
Prasanta Gorai https://orcid.org/0000-0003-1602-6849
Olli Sipilä https://orcid.org/0000-0002-9148-1625
Kazuhito Dobashi https://orcid.org/0000-0001-8058-8577
Paola Caselli https://orcid.org/0000-0003-1481-7911
Tirupati Kumara Sridharan https://orcid.org/0000-0001-5921-5784
Tomomi Shimoikura https://orcid.org/0000-0002-1054-3004
Jonathan C. Tan https://orcid.org/0000-0002-3389-9142

References

Benjamin, R. A., Churchwell, E., Babler, B. L., et al. 2003, PASP, 115, 953
Bonfand, M., Csengeri, T., Bontemps, S., et al. 2024, A&A, 687, A163
Burkhardt, A. M., Herbst, E., Kalenskii, S. V., et al. 2018, MNRAS, 474, 5068
CASA Team, Bean, B., Bhatnagar, S., et al. 2022, PASP, 134, 114501
Chapman, J. F., Millar, T. J., Wardle, M., Burton, M. G., & Walsh, A. J. 2009, MNRAS, 394, 221
Cyganowski, C. J., Brogan, C. L., Hunter, T. R., & Churchwell, E. 2009, ApJ, 702, 1615
Cyganowski, C. J., Whitney, B. A., Holden, E., et al. 2008, AJ, 136, 2391
Endres, C. P., Schlemmer, S., Schilke, P., Stutzki, J., & Müller, H. S. P. 2016, JMoSp, 327, 95
Fazio, G. G., Hora, J. L., Allen, L. E., et al. 2004, ApJS, 154, 10
Fedriani, R., Tan, J. C., Telkamp, Z., et al. 2023, ApJ, 942, 7
Giannetti, A., Leurini, S., König, C., et al. 2017, A&A, 606, L12
Green, C.-E., Green, J. A., Burton, M. G., et al. 2014, MNRAS, 443, 2252
Griffin, M. J., Abergel, A., Abreu, A., et al. 2010, A&A, 518, L3
Hassel, G. E., Herbst, E., & Garrod, R. T. 2008, ApJ, 681, 1385
Herbst, E., & van Dishoeck, E. F. 2009, ARA&A, 47, 427
Hernández-Hernández, V., Zapata, L., Kurtz, S., & Garay, G. 2014, ApJ, 786, 38
Hoque, A., Baug, T., Dewangan, L. K., et al. 2025, ApJ, 987, 197
Hunter, T. R., Brogan, C. L., Cyganowski, C. J., & Young, K. H. 2014, ApJ, 788, 187
Juvela, M., & Ysard, N. 2011, ApJ, 739, 63
Li, C., Qin, S.-L., Liu, T., et al. 2024, MNRAS, 533, 1583
Ossenkopf, V., & Henning, T. 1994, A&A, 291, 943
Peng, Y., Liu, T., Qin, S.-L., et al. 2022, MNRAS, 512, 4419
Pickett, H. M., Poynter, R. L., Cohen, E. A., et al. 1998, JQSRT, 60, 883

Sakai, N., Sakai, T., Hirota, T., & Yamamoto, S. 2008, ApJ, 672, 371
Sakai, N., & Yamamoto, S. 2013, ChRv, 113, 8981
Suzuki, H., Yamamoto, S., Ohishi, M., et al. 1992, ApJ, 392, 551
Taniguchi, K., Gorai, P., & Tan, J. C. 2024a, Ap&SS, 369, 34
Taniguchi, K., Gorai, P., Tan, J. C., et al. 2024b, A&A, 692, A65
Taniguchi, K., Herbst, E., Caselli, P., et al. 2019a, ApJ, 881, 57
Taniguchi, K., Herbst, E., Majumdar, L., et al. 2021, ApJ, 908, 100
Taniguchi, K., Majumdar, L., Caselli, P., et al. 2023a, ApJS, 267, 4
Taniguchi, K., Miyamoto, Y., Saito, M., et al. 2018a, ApJ, 866, 32
Taniguchi, K., Ozeki, H., Saito, M., et al. 2016a, ApJ, 817, 147
Taniguchi, K., Saito, M., Hirota, T., et al. 2017, ApJ, 844, 68
Taniguchi, K., Saito, M., Majumdar, L., et al. 2018c, ApJ, 866, 150
Taniguchi, K., Saito, M., & Ozeki, H. 2016b, ApJ, 830, 106
Taniguchi, K., Saito, M., Sridharan, T. K., & Minamidani, T. 2018b, ApJ, 854, 133
Taniguchi, K., Saito, M., Sridharan, T. K., & Minamidani, T. 2019b, ApJ, 872, 154
Taniguchi, K., Sanhueza, P., Olguin, F. A., et al. 2023b, ApJ, 950, 57
Telkamp, Z., Fedriani, R., Tan, J. C., et al. 2025, ApJ, 986, 15
Terebey, S., Chandler, C. J., & Andre, P. 1993, ApJ, 414, 759
Vastel, C., Bottinelli, S., Caux, E., Glorian, J.-M., & Boiziot, M. 2015, in SF2A-2015: Proc. the Annual Meeting of the French Society of Astronomy and Astrophysics, ed. F. Martins et al., 313
Werner, M. W., Roellig, T. L., Low, F. J., et al. 2004, ApJS, 154, 1
Zhang, Y., & Tan, J. C. 2018, ApJ, 853, 18